

DYNAMIC RUPTURE IN A LAYERED MEDIUM: THE 1966 PARKFIELD EARTHQUAKE

BY RALPH J. ARCHULETA AND STEVEN M. DAY

ABSTRACT

A method for computing ground motion from a propagating stress relaxation in a vertically heterogeneous medium was developed wherein computational efficiency is enhanced by separating the source, a three-dimensional calculation, from the wave propagation, a two-dimensional calculation. As an application of this technique, displacement-time histories were computed corresponding to those determined from accelerograms recorded during the 1966 Parkfield, California earthquake. On the basis of these comparisons, an effective stress of 25 bars, an average slip of 43 cm, and a moment of 2.32×10^{25} dyne-cm were determined for the Parkfield earthquake.

INTRODUCTION

In the analysis of ground motion resulting from an earthquake, it is always possible to match the recorded motion with a synthetic record. The more records that exist, the more difficult the match. A perfect match between the recorded data and synthetics does not guarantee a unique interpretation of the earthquake mechanism. Motion resulting from an earthquake is a convolution of the earthquake mechanism and the propagation path between source and receiver. In generating a synthetic record, one can assign complexities to the earthquake mechanism that in fact arose from the propagation path and vice versa. This tradeoff between source and path can be limited where the elastic properties of the medium are independently determined, e.g., by a seismic-refraction profile. It is easy to see how inferences as to the nature of an earthquake mechanism might be strongly biased by the assumptions used in the analysis of an earthquake.

In this paper is described a method for generating synthetic records of the time history of ground motion produced by an earthquake. Bearing in mind the non-uniqueness of any synthetic record, the primary guideline is to maximize the physics of an earthquake in the model and the description of the medium in the propagation. The earthquake mechanism is represented as a propagating stress relaxation over a finite fault and the medium as a horizontally layered elastic continuum. A three-dimensional finite element method is used to compute the displacement discontinuity associated with the faulting; a two-dimensional finite element method is used to compute the Green's functions for the medium. Using these two parts in the elastodynamic representation theorem, the near-field ground displacement is computed. As an example of this method, a simulation of the 1966 Parkfield, California earthquake is made. In this process, the best match between the data records and our synthetic records are not sought by adjusting the free parameters in our method. Rather, the closeness of the match is viewed as an illustration of how a rather simple physical description of an earthquake mechanism coupled with a reasonable approximation to the medium produces realistic ground motion.

PHYSICAL MODEL

The physics of the earthquake mechanism is simulated by a propagating stress relaxation with the properties of the medium assuming homogeneous horizontal

layers of elastic material overlying a half-space. Following Archuleta and Frazier (1978), the earthquake mechanism is simulated by specifying: (1) the hypocenter, the geometry of the final fracture surface, and the constitutive properties of the medium; (2) a rupture velocity, v , that determines the evolution of the fracture process; (3) an initial stress tensor $S^0(x)$ in the medium from which one can derive the initial tractions on the fracture plane; and (4) the frictional tractions that will oppose the motion as the two sides of the fault slip past each other.

Rupture Process. The rupture initiates at the hypocenter, i.e., the stress drops from its initial value to the sliding friction value. The stress relaxation spreads over the fault plane with the given constant velocity, assumed to be less than the shear-wave speed B of the medium. As the rupture front encompasses new area of the fault plane, this new area undergoes an immediate stress relaxation, a dynamic stress drop—the sum of the effective stress (the difference between the initial stress and the sliding frictional stress), and the stress due to prior radiation. (Stress relaxation or stress buildup refers only to the components of the stress tensor tangent to the fault plane.) The stress due to prior radiation is a critical element of the stress relaxation mechanism and is absent from kinematic models. Prior radiation stress is a consequence of the rupture velocity being less than the shear-wave speed of the medium. As the rupture propagates, the changes in the stress field are transmitted throughout the medium with the speeds of the elastic waves of the medium. Since the rupture is subsonic ($v < B$) and there is no tangential displacement on the fault plane until the rupture front arrives, stress ahead of the rupture front and on the fault plane increases above its initial value as stress relaxation occurs on other parts of the fault plane. The focusing of energy in the direction of propagation is a combination of both directivity (Ben-Menahem, 1961) and prior radiation stress.

The time when a point on the fault surface undergoes a dynamic stress drop is precisely determined by its distance from the hypocenter and the rupture velocity. The time when a particle attains its static displacement, however, is determined by the instantaneous stresses and inertial forces acting on the particle. When the force due to the instantaneous stress plus the force due to inertia acting on a particle is less than the force due to sliding friction, the slip velocity is set to zero and the dislocation is held fixed (i.e., the fault is healed). Without healing, the slip velocity would reverse its direction, and sliding friction would become the driving mechanism for the equations of motion.

A major difficulty in the computation of the slip function is the implementation of the stopping criterion. Because the numerical method of Archuleta and Frazier (1978) depends on discrete time intervals, driving forces in the medium and the force due to sliding friction are not simultaneously known. In order to compare these two forces at the same time, two coupled nonlinear equations are solved (see Appendix).

METHOD

The method for computing the complete ground motion is based on dividing the problem into two parts: (1) computing the fault slip function and (2) propagating the waves from source to receiver. The first procedure requires a fully three-dimensional numerical treatment, whereas the second is reduced to a two-dimensional computation. By partitioning the problem in this manner rather than directly computing ground motion from a three-dimensional calculation, the cost of the overall computation is reduced by two orders of magnitude. The basis for our approach is the elastodynamic representation theorem (Maryuama, 1963; Burridge

and Knopoff, 1964). In a medium with spatial coordinates defined relative to orthonormal basis vectors $\hat{x}_1, \hat{x}_2,$ and \hat{x}_3 the displacement of a particle

$$u_m(\mathbf{x}, t) = \int_{t'} \int_{\Sigma(t')} \hat{\mathbf{n}}(\boldsymbol{\xi}) \cdot \mathbf{T}^{(m)}(\boldsymbol{\xi}, \mathbf{x}; t, t') \cdot \mathbf{s}(\boldsymbol{\xi}, t) dt d\xi, \tag{1}$$

where $u_m(\mathbf{x}, t)$ is the m th component of displacement for a particle located at \mathbf{x} at time t ; and $\mathbf{s}(\boldsymbol{\xi}, t)$ is the discontinuity in displacement at position $\boldsymbol{\xi}$ at time t' . $\Sigma(t')$ is the area over which $\dot{\mathbf{s}}(\boldsymbol{\xi}, t')[\dot{\mathbf{s}}(\boldsymbol{\xi}, t) = \partial/\partial t \mathbf{s}]$ is nonzero; $\hat{\mathbf{n}}(\boldsymbol{\xi})$ is a unit vector normal to $\Sigma(t')$ at position $\boldsymbol{\xi}$; $\mathbf{T}^{(m)}(\boldsymbol{\xi}, \mathbf{x}; t, t')$ is a stress tensor at position \mathbf{x} and time t resulting from a unit force located at $\boldsymbol{\xi}$ and time t' acting in the m th direction. The ij component (relative to $\hat{x}_1, \hat{x}_2, \hat{x}_3$) of the tensor $\mathbf{T}^{(m)}(\boldsymbol{\xi}, \mathbf{x}; t', t)$, hereafter \mathbf{T}^m , is given by

$$\mathbf{T}_{ij}^{(m)} = C_{ijkl} G_{km,l}(\boldsymbol{\xi}, \mathbf{x}; t', t) \tag{2}$$

where $i, j, k, l, m = 1, 2, 3$ and summation over repeated indices is assumed. C_{ijkl} is an elastic tensor, and $G_{mk,l}(\boldsymbol{\xi}, \mathbf{x}; t', t)$ is the spatial derivative in the x_l direction of the mk component of the Green's function solution $G(\boldsymbol{\xi}, \mathbf{x}; t', t)$ for a particle located at \mathbf{x} and time t due to a point force in the m th direction located at $\boldsymbol{\xi}$ acting at time t' .

If one were to specify $\mathbf{s}(\boldsymbol{\xi}, t')$ before the rupture occurs and without regard to the tractions acting on the fault during the rupture process, the earthquake would be simulated as a kinematic source. Here, $\mathbf{s}(\boldsymbol{\xi}, t')$, determined by a propagating stress relaxation is used; hence, the earthquake is simulated as a dynamic source mechanism. The Green's function $G(\boldsymbol{\xi}, \mathbf{x}; t', t)$ is known analytically for a homogeneous full-space and half-space; thus, $\mathbf{T}^{(m)}$ is readily calculated for these idealized geometries. For an inhomogeneous medium, such as a horizontally layered medium, however, the Green's function is not known analytically and must be computed for a specific structure. Once $\mathbf{s}(\boldsymbol{\xi}, t')$ and $\mathbf{T}^{(m)}$ are known, the integration in equation (1) is performed numerically for each observation point.

The procedure we have employed for synthesizing near-field ground motion minimizes the computing cost for a given frequency resolution of ground motion. Since the frequency resolution of the computed slip function is about four times better than the normal finite element resolution (Archuleta and Frazier, 1978), a two-dimensional grid is used in computing $\mathbf{T}^{(m)}$ with four times the spatial density used in the three-dimensional grid, thereby increasing the frequency resolution of the elastic waves propagated into the medium without a commensurate increase in cost.

Computing the Green's function [or $\mathbf{T}^{(m)}$]. Note that a horizontally layered medium does not affect the azimuthal radiation pattern generated by a point force. In a polar coordinate system, $(\hat{r}, \hat{\theta}, \hat{z})$ where \hat{z} is the downward vertical direction, only the \hat{r} and \hat{z} dependence of $\mathbf{T}^{(m)}$ must be computed. Hence, the computation of $\mathbf{T}^{(m)}$ is two-dimensional, whereas $\mathbf{s}(\boldsymbol{\xi}, t)$ is three-dimensional.

To compute $\mathbf{T}^{(m)}$, a vertical point force is applied at the origin of the cylindrical system in which the elastic properties of the medium vary only with depth (z). The finite element method is used to determine a stress tensor $\mathbf{T}^{(z)}(r, z)$ throughout the medium. Then, a horizontal point force is applied at the origin to compute $\mathbf{T}^{(r)}(r, z)$. Using $\mathbf{T}^{(z)}$ and $\mathbf{T}^{(r)}$ plus *a priori* knowledge of the azimuthal component, $\mathbf{T}^{(m)}$ is completely determined for the medium.

APPLICATION: 1966 PARKFIELD EARTHQUAKE

The 1966 Parkfield, California earthquake (June 28, 4:26:14 GMT) is well-known for the quality and quantity of the strong-ground-motion records it produced (Cloud and Perez, 1967). Many workers (e.g., Aki, 1968; Haskell, 1969; Boore *et al.*, 1971; Trifunac and Udvardi, 1974; Anderson, 1974; Levy and Mal, 1976) have attempted to match the displacement records with synthetic records generated by a simulation of the Parkfield earthquake by specifying a propagating displacement discontinuity over a prescribed fault plane embedded within a homogeneous full-space. The effect of traction-free surface has usually been accounted for by doubling the displacement amplitude, although Levy and Mal (1976) rigorously accounted for the free surface by employing the Green's functions for a half-space. Here the Parkfield earthquake

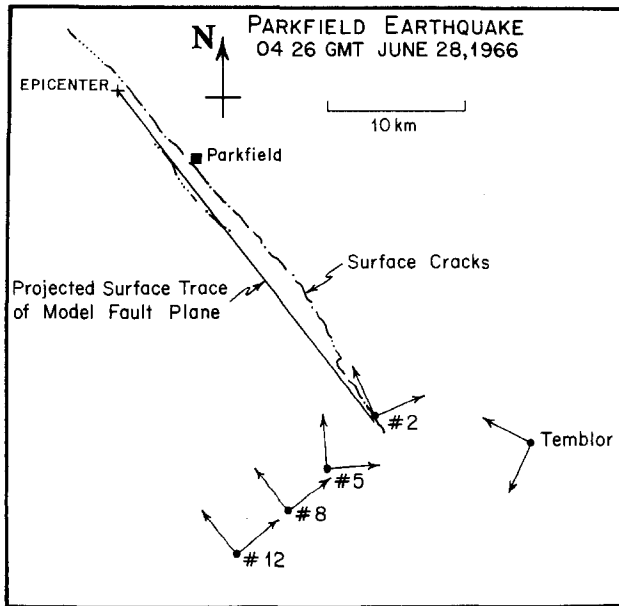


FIG. 1. The projected trace of the rupture relative to the location of the strong-motion accelerometers.

is simulated as a propagating stress relaxation over a prescribed fault plane embedded within a horizontally layered medium. A three-dimensional finite element method is used to determine the displacement discontinuity associated with the faulting; then, near-field seismograms are computed by means of the elastodynamic representation theorem. We seek to determine to what extent a simple propagating stress relaxation model of faulting can reproduce significant features of the near-field observations.

A good summary of the Parkfield earthquake and of early attempts to match the displacement records is given by Trifunac and Udvardi (1974). The 1966 Parkfield earthquake was primarily a right-lateral strike-slip rupture occurring on the San Andreas Fault (McEvelly *et al.*, 1967). The aftershocks define a plane dipping 86° SW and striking $N39^{\circ}$ W (Eaton *et al.*, 1970). The aftershocks extend from the surface to a depth of about 14 km and over a length of about 37 km (Eaton *et al.*, 1970). Rupture nucleated at $35^{\circ} 57.3'N$, $120^{\circ} 29.9'W$ (McEvelly, 1966) and propagated primarily to the southeast toward the Cholame-Shandon array of accelerometers, henceforth referred to as stations 2, 5, 8, 12, and Temblor (see Figure 1). The component of particle displacement approximately perpendicular to the strike of the fault (hereafter referred to as the transverse component) had the largest

amplitude at each station (Housner and Trifunac, 1967). Surficial displacement of 4.5 cm occurred at the southeastern end of the fault within 10 hr of the earthquake (Allen and Smith, 1966). In the year following the earthquake, accumulated displacement parallel to the strike of the fault was measured within 100 m of the fault, trace was 21 cm (Smith and Wyss, 1968). The geology near the fault and the accelerographs indicate structure varying with depth (Eaton *et al.*, 1970) and horizontal structure (Aki, 1969), which clearly influenced the recorded ground motion.

On the basis of the aftershock distribution (Eaton *et al.*, 1970), a fault plane 30 km long and 6 km wide between 3- and 9-km depth is specified. The surface trace of the fault plane is shown in Figure 1 along with the location of the accelerograph stations. The strike of the fault is assumed to be N40°W with a dip of 90°. The hypocenter is placed at the north end at a depth of 7 km. Rupture spreads over the prescribed fault surface at a velocity of 3.1 km/sec (0.9B), propagating toward the accelerograph stations. The effective stress σ_e is assumed to be constant over the fault plane. As the numerical solution scales with σ_e , (Archuleta and Frazier, 1978) the effective stress is determined by matching synthetic and observed peak-displacement amplitudes for the N85°E component at station 5. The effective stress

TABLE 1
ASSUMED PARKFIELD STRUCTURE

Depth Range (km)	P Wave (km/sec)	S Wave (km/sec)	Shear Modulus (bars)
0-2	3.0	1.73	0.5×10^5
2-4	5.0	2.89	1.9×10^5
4-∞	6.0	3.46	3.09×10^5

determined in this manner is 25 bars, and the results presented have been scaled to this value. As the curves of Figure 4 show, the static-stress drop over most of the fault plane is nearly identical to the effective stress.

Near the fault, the detailed structure given in Eaton *et al.* (1970) is approximated by two layers over a half-space (Table 1) for the wave propagation calculation. For the three-dimensional computation of the slip function, a homogeneous half-space is used with the same material properties as the underlying half-space given in Table 1. Since most of the prescribed fault surface lies in the underlying half-space, this simplification is probably not important for defining the slip function. In any case, because of the coarse gridding of the source computation, there would have been little resolution of the layers.

Motion on the fault surface. To illustrate the particle motion on the fault, Figures 2 and 3 show the particle displacements and particle velocities along the fault at the depth of the hypocenter. Both the particle displacement and particle velocity increase in the direction of the rupture propagation. Note that the increase in amplitudes does not persist all the way to the end of the fault. The amplification of the particle velocity exists for a distance equivalent to about two widths. The width of the faulting area directly affects the time duration of the particle velocity. Once the area over which the stress can relax is restricted, the effect of the boundary is to limit the particle velocity in amplitude and time duration. The plots of Figure 5 clearly demonstrate that only a small part at the total fault plane acts at any given time. By matching the peak amplitude of the synthetic seismogram with the measurement at station 5, it is found that $\sigma_e = 25$ bars, thus giving an average displacement of 2.5 cm (slip = 43 cm).

In Figure 4, the stress component S_{31} was plotted as a function of position along

the fault at successive times during the rupture process. The discrete points on the fault are all at the same depth as the hypocenter. The primary feature of Figure 4 is that the stress relaxes to the value of sliding friction. There is marked finite increase in the stress S_{31} above the initial value S_{31}^0 ahead of the rupture front. Although most of the fault remains at the frictional stress level, the southeastern end of the fault relaxes beyond the frictional level. This excess relaxation is attributed to the abrupt ending of the fault; i.e., no slip is allowed to occur outside the prescribed final fault boundaries.

Healing of the fault is illustrated in Figure 5. The shaded area represents that part of the fault where slip is occurring at the time shown at the right. For example,

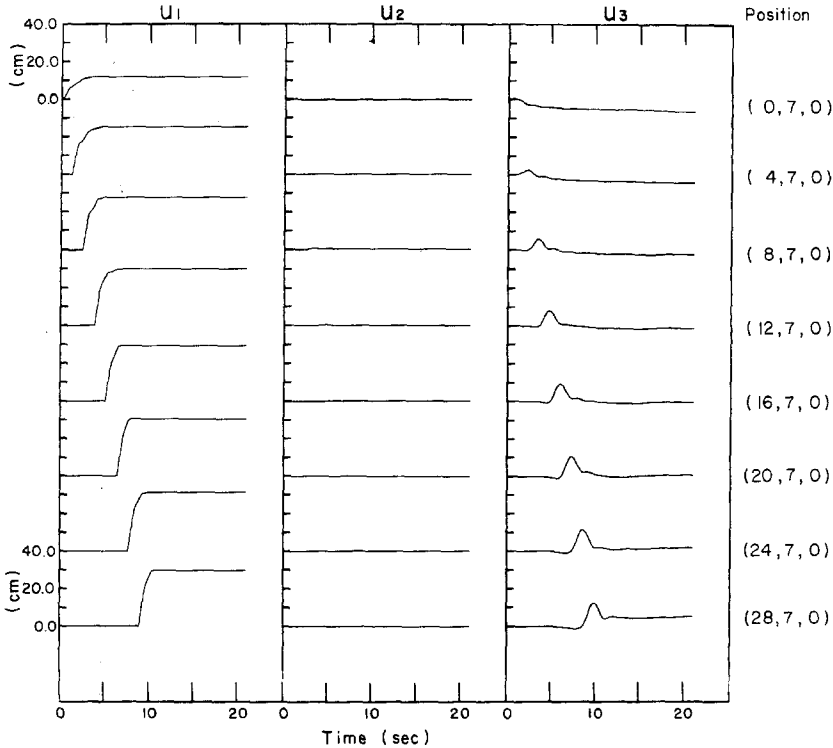


FIG. 2. Three components of particle displacement on the fault surface extending along the strike of the fault and at the depth of the hypocenter. U_1 is parallel to the strike of the fault, U_2 is vertical, and U_3 is normal to the fault plane.

at 6 sec after rupture initiation, that portion of the fault between about 6 and 18 km has a nonzero slip velocity. During the rupture, only part of the total fracture surface has a nonzero slip rate. As the fracture propagates, it creates new surface area that has a nonzero slip rate, but the boundaries of the fault are causing the fault to heal behind the rupture front, thereby producing a slipping section that propagates along the fault similar to a model proposed by Mansinha (1964). Although a real earthquake may not have such well-defined boundaries, some boundary does limit the width of faulting. Because there is no compelling evidence of breaking the free-surface depth during the 1966 Parkfield earthquake, it is reasonable to assume that rupture did not extend to the surface during the time of rupture propagation. Certainly in cases where the length of faulting is much greater than the depth, e.g., the 1906 California earthquake, it seems physically unreasonable to require that slip at the hypocenter continues for the full duration of rupture. Some type of a moving

section of nonzero slip rate, is then appropriate for earthquakes with large length-to-width ratios. Rupture reaches the point farthest from the hypocenter after 9.8 sec, and the entire fault has healed by 10.4 sec.

Free surface deformation. Before examining the individual displacement records at stations 2, 5, 8, and 12, the overall deformation of the free surface is considered. As a measure of this deformation, contour plots of the maximum transverse particle velocity (Figure 6) and the static displacement parallel to the strike of the fault (Figure 7) were constructed. As a reference for the contours, a selection was made of the maximum value attained anywhere on the free surface, as indicated in the

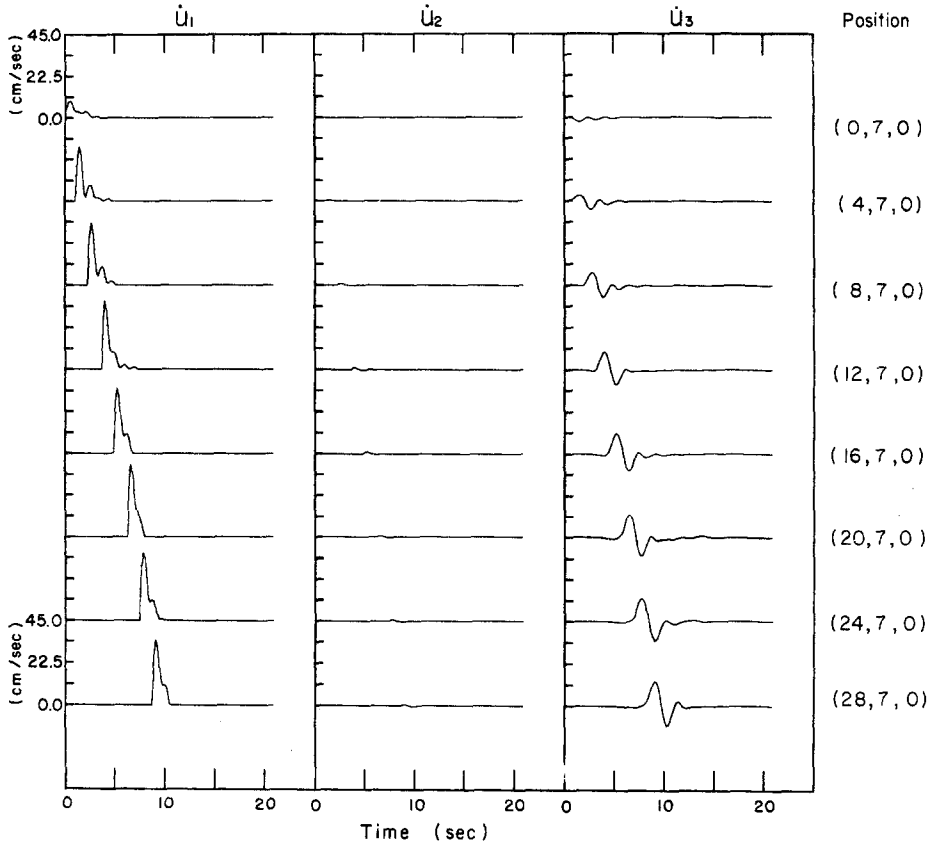


FIG. 3. The three components of particle velocity corresponding to the displacements shown in Figure 2.

figure caption. The contours are then drawn as 90, 80, 70 per cent, ... of this maximum. They are approximate in that particle motion is appropriate for a homogeneous half-space. The contours thus primarily represent the body-wave contribution to the motion. The maximum scales directly with σ_E , the effective stress.

The contours representing the maximum values of the transverse particle velocity are shown in Figure 6. Two features stand out: (1) the focusing of energy in the direction of propagation and (2) the broad maximum at the stopping end of the fault. The focusing is less evident in the parallel-particle velocity. The broad 90 per cent contour in Figure 9 encompasses both stations 2 and 5. If the effect of layering is neglected, both stations would receive nearly the same peak-particle velocity. Station 2 was chosen to be right above the stopping end.

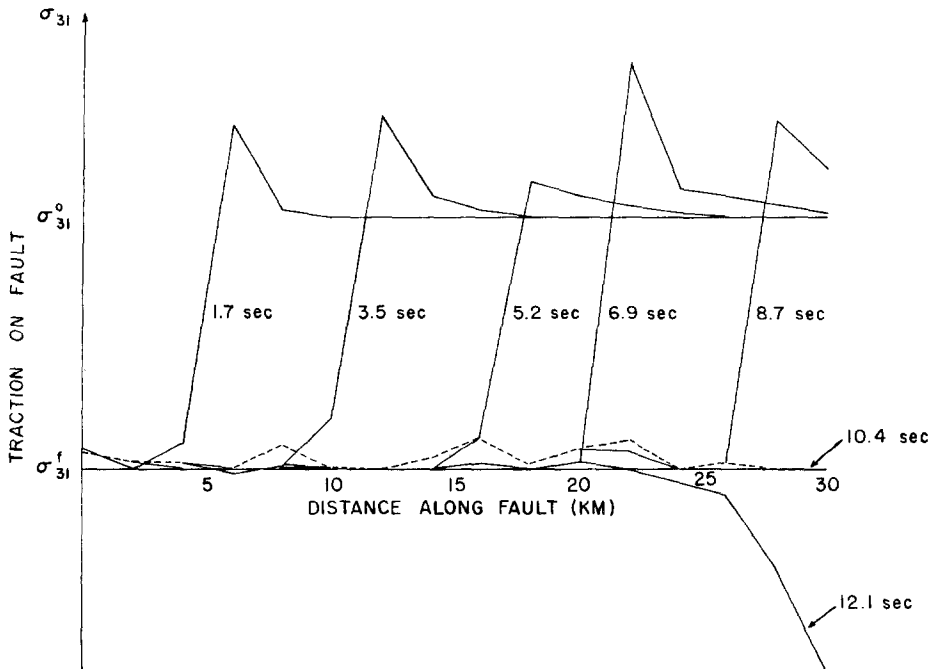


FIG. 4. Shear-stress component S_{31} taken along the strike of the fault at the locations of the particle displacement and particle velocity shown in Figures 2 and 3 for successive time during the rupture. (Before the rupture starts, every point is at level S_{31}^0 .) As the rupture propagates along the strike, the shear stress relaxes to the sliding friction. The increase in S_{31} above the level S_{31}^0 is produced by prior radiation described in the text. The dashed line at 10.4 sec represents a time immediately preceding the final healing of the fault. The snapshot is at 12.1 sec, after the fault has healed everywhere, and represents the static-stress drop.

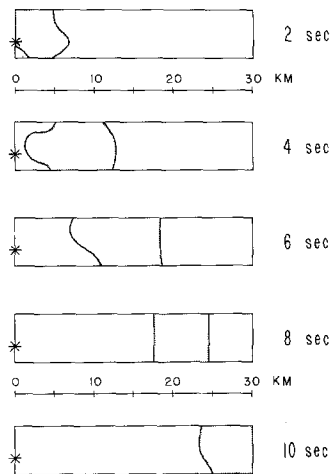


FIG. 5. Growth of the rupture zone with time. The shaded area represents that part of the fault over which the slip is occurring. The fault heals behind the rupture front. The length of fault on which slip is occurring is roughly equal to the width of the fault.

In Figure 7, the contours for the component of static displacement parallel to the strike of the fault are shown. Note that the maximum value occurs approximately 6 to 8 km off the fault (within the 90 per cent contour). The relative motion between the two sides of the fault caused by the simulated earthquake is approximately 16

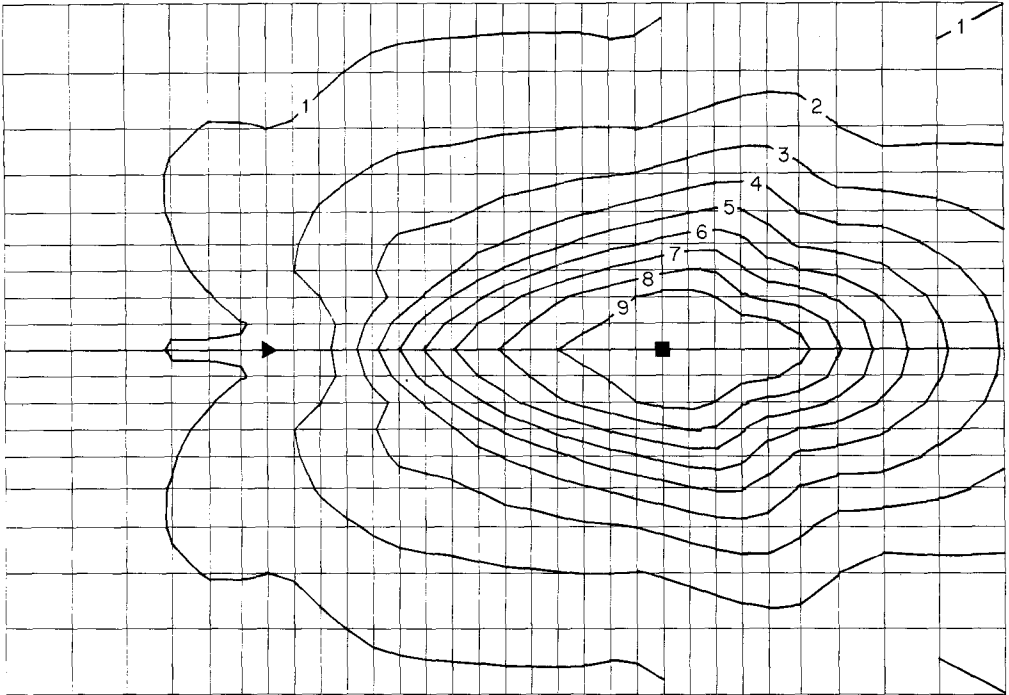


FIG. 6. Contours of normal component of particle velocity maxima. Solid triangle is at the epicenter, and solid square designates the southeast end of the projected fault trace. Contour labels 9, 8, 7, ... represent 90, 80, and 70 per cent of the maximum value reached anywhere on the free surface. In this case, the maximum is 6.9 cm assuming a 25-bar effective stress.

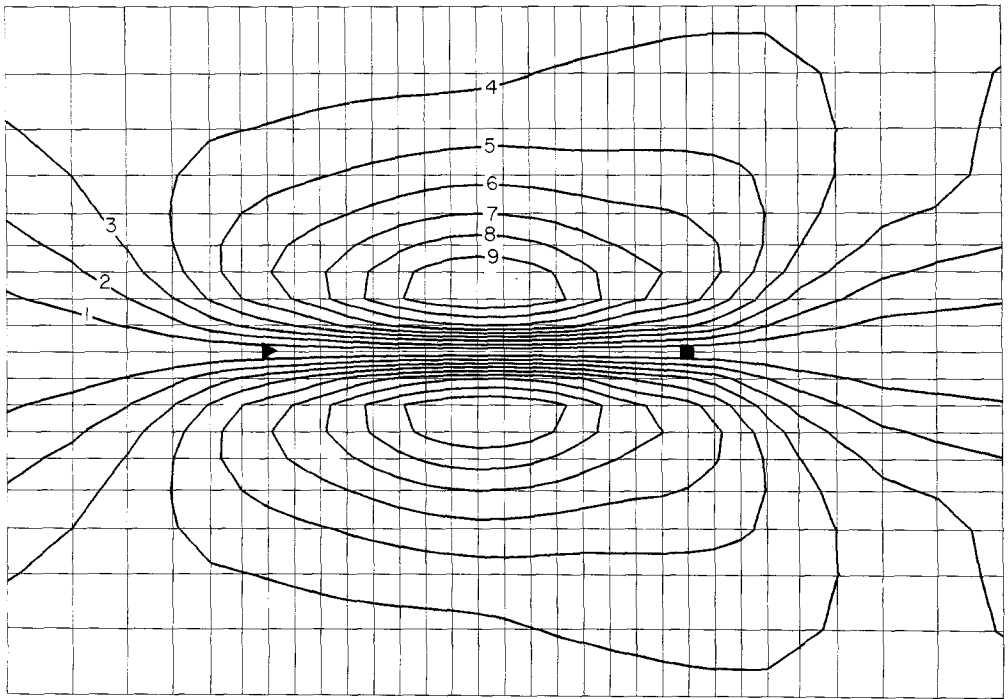


FIG. 7. Contours of the parallel component of static displacement on the free surface. The maximum is 6.9 cm. See Figure 6 caption for explanation of contour labels.

cm (using the 90 per cent contour). Sixteen centimeters is quite close to the geodetic value of 20 cm found by the California Department of Water Resources, also 6 to 8 km from the fault and in approximately the same area encompassed by the 90 per cent contour. Taking into account that the half-space has a greater shear modulus than the near-surface layers, the computed values were expected to be low. Note also the strain concentration near the strike of the fault, which results directly from the fact that the rupture surface is buried. If all the strain were relieved, then the total cumulative displacement near the center of the strike would be about 17 cm,

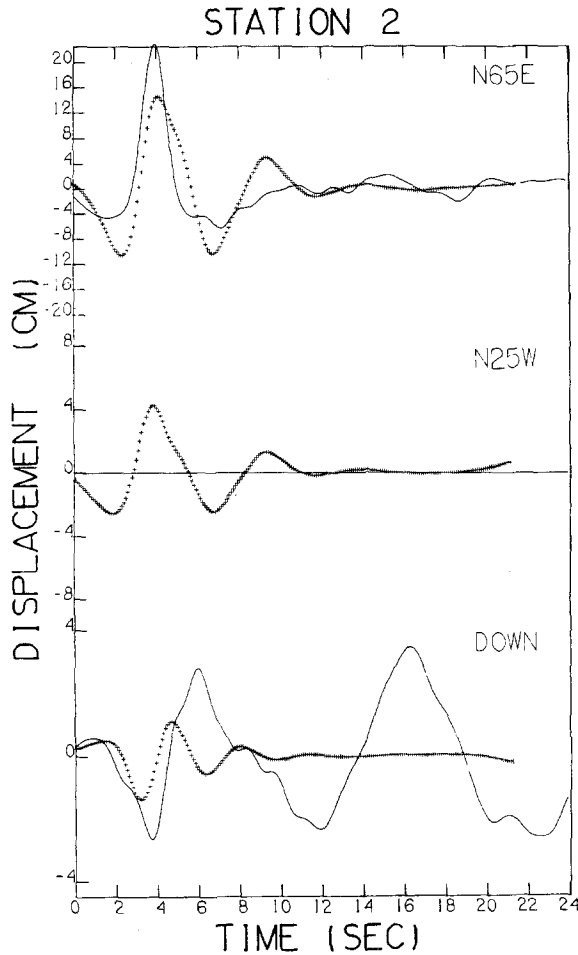


FIG. 8. Recorded (solid line) and synthetic (crosses) displacements for station 2.

in good agreement with the 21 cm of postseismic relative displacement found by Smith and Wyss (1968).

From these admittedly rough approximations to the actual ground motion, certain conclusions can be drawn. The creep measurements following the 1966 Parkfield earthquake are consistent with a rupture that did not reach the surface, thereby concentrating strain in the upper kilometers. The transverse component of motion dominated the free-surface motion. The accelerometers were situated to receive nearly a maximum in ground motion, assuming our fault geometry is approximately correct.

Stations 2, 5, 8, and 12. By the curves of Figures 8, 9, 10, and 11, the observed (solid line) and synthetic (crosses) displacements at stations 2, 5, 8, and 12 can be compared. The displacement data comes from twice integrating the instrument-corrected accelerograms and have been bandpassed using an Ormsby filter, $f_c = 0.12$ Hz and $f_T = 0.10$ Hz (Trifunac, 1971). The same filter was applied to the synthetic records. In order to minimize any error due to numerical dispersion, the synthetic records were low-passed with a cut-off frequency of 0.5 Hz. The same low-pass filter

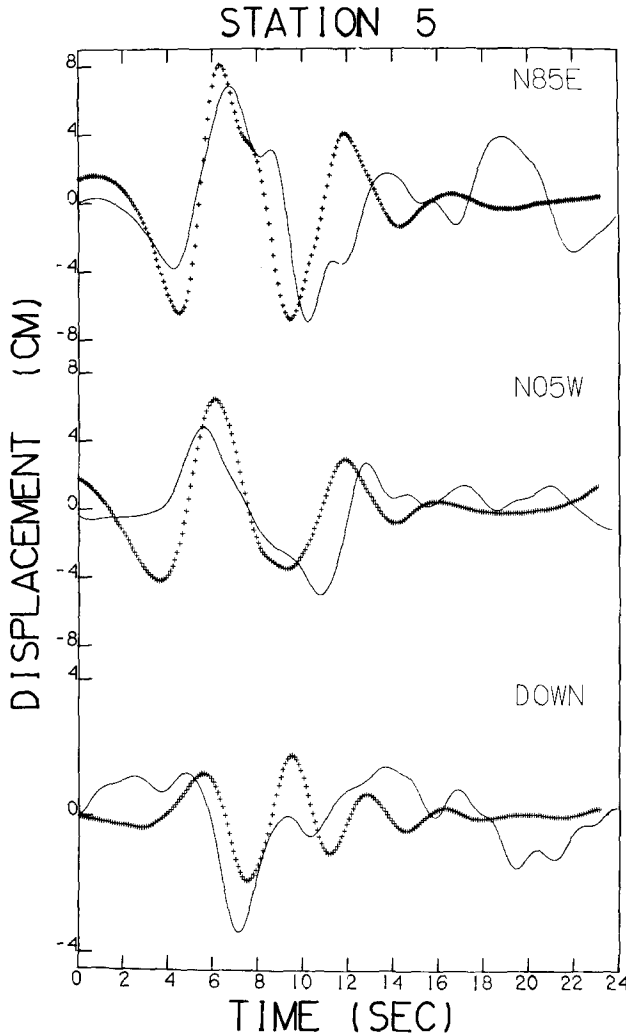


FIG. 9. Recorded (solid line) and synthetic (crosses) displacements for station 5. See Figure 11 caption.

was applied to the data. Thus the data and synthetics are compared within the same frequency band. Since absolute timing is not available for the observed records, the times shown in Figures 8 to 11 are relative to the trigger times of the instruments. The time origin of the synthetic records were shifted for each station to obtain the best agreement with the observed records (at any given station, of course, all three components are shifted by the same amount). In so doing, inferences relative to the

earthquake origin time were made with trigger times of 8.2 sec at station 2, 6.2 sec at station 5, 9.5 sec at station 8, and 8.7 sec at station 12.

Taken as a group, the curves of Figures 8, 9, 10, and 11 show two encouraging aspects: (1) at a given station, relative amplitudes, and to a considerable degree, the phases, have been reproduced; and (2) the relative amplitudes were matched fairly well among the stations. Overall, the agreement during the first 12 sec or so is satisfying; in detail, some discrepancies are obvious.

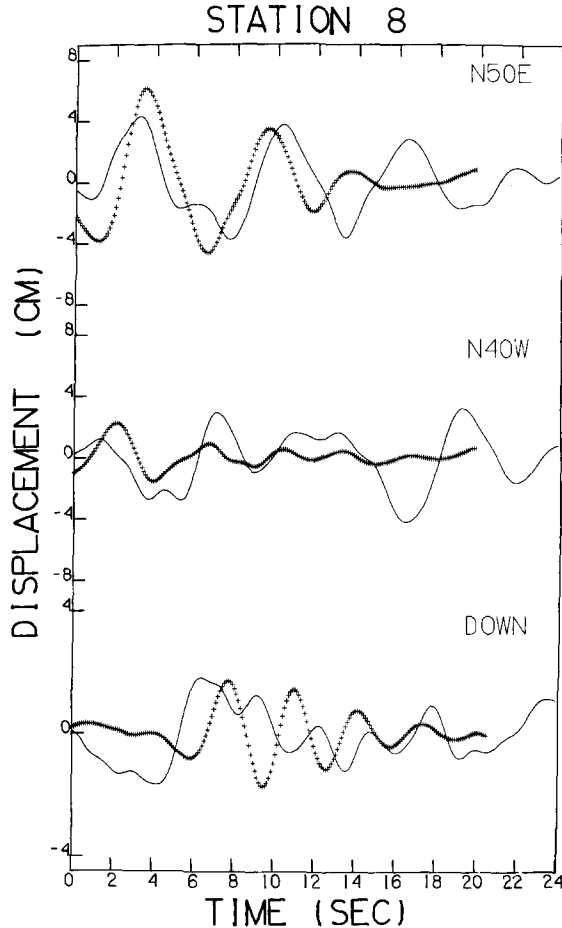


FIG. 10. Recorded (solid line) and synthetic (crosses) displacements for station 8.

Station 2 deserves particular consideration. Note from Figure 1 that the fault was placed such that its surface projection lies slightly to the southwest of station 2. This is contrary to geomorphic evidence; surface breaks associated with the San Andreas Fault are observed several hundred meters northeast of station 2. This slight adjustment of the fault plane was required in order to obtain agreement between the synthetic and observed waveforms in the vertical component at station 2. The polarity of the synthetic vertical record would be inverted if the fault-plane projection, a nodal plane for vertical motion, coincided with the mapped surface trace. The small shift of the fault has no effect on the transverse component of motion (parallel to the fault normal) since that component is symmetric with respect

to the fault plane. One explanation for the polarity of the vertical component would be that the surface break does not coincide with the surface projection of the buried rupture plane. An alternative explanation would be that the surface break actually does represent the surface projection of the buried plane of rupture, but a lateral contrast in seismic velocities across the fault has slightly distorted the radiation pattern. Such radiation pattern distortion has been documented by McNally and McEvelly (1977) for other sections of the central San Andreas and interpreted by

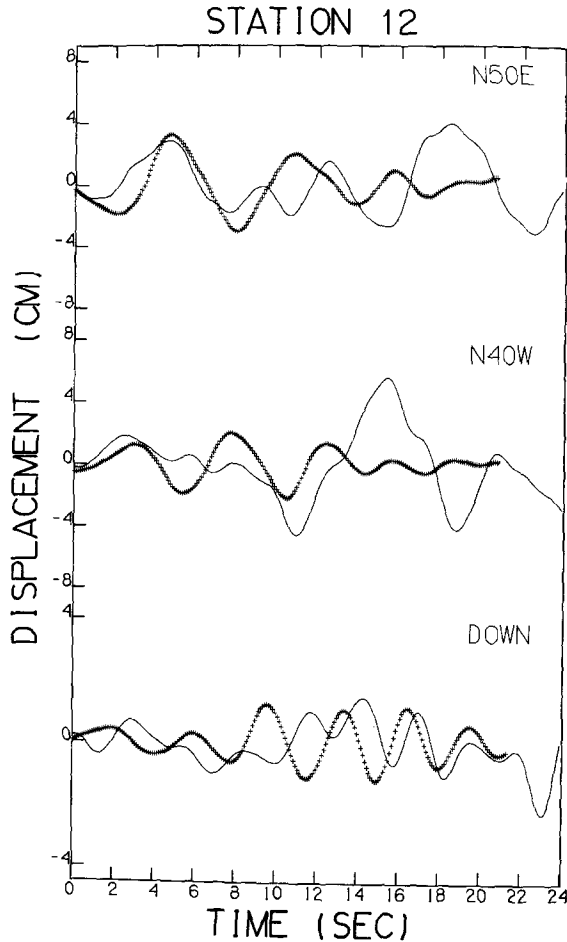


FIG. 11. Recorded (solid line) and synthetic (crosses) displacements for station 12.

them in terms of lateral refraction. Either explanation seems adequate to explain the initial part of the waveform of the vertical component at station 2.

For the NE component at station 2, observed and synthetic displacement records are nearly identical in maximum peak-to-peak amplitude but disagree by about 35 per cent in maximum displacement. For the synthetic records, the maximum transverse displacement at station 2 exceeds that at station 5 by about 50 per cent (after accounting for accelerometer orientation). This enhancement at station 2 is an effect of the layering, since the uniform half-space results have similar transverse displacement maxima at stations 2 and 5.

Unaccounted for by the simulation is the long-period motion at station 2 beginning

TABLE 2
SOURCE PARAMETERS FOR 1966 PARKFIELD EARTHQUAKE

	α (km/sec)	β (km/sec)	L (km)	W (km)	v (km/sec)	s (cm)	M_0 ($\times 10^{25}$ dyne-cm)*	σ_E (bars)	
Archuleta and Day	6.0	3.46	30	6	3.1	43	2.32	25	Layered structure. Half-space values.
Levy and Mal (1976)	5.6	3.23	38	6	2.4	200	13.7		Bilateral: 5 km NW, 33 km SE. Half-space calculation.
Trifunac and Udvardia (1974)	5.6	3.23	35	6	2.3-2.5	66	4		
Anderson (1974)	6.0	3.46	38	8	2.8-3.0	50	4.56		Bilateral: 5 km NW, 33 km SE, km SE.
Boore, Aki, and Todd (1971)	6.0	3.5	33	3	2.2	70-100	1.96-2.8		
Haskell (1969)	4.95	2.86	20	5	2.2	93	2.79		
Aki (1968)	6.0	3.5	33	3	2.2	50	1.4		Determined from measure value of moment 1.4×10^{25} .
Wu (1968)			35	5				~10-33	Dislocation varies with depth.

* $M_0 = (0.93-2.07) \times 10^{25}$ dyne-cm Tsai and Aki (1968).

+ $\mu = 3 \times 10^{11}$ dyne/cm² assumed

at about 12 sec. The disturbance has an amplitude of about 4 cm on the vertical component and 2 cm on the transverse (NE) component. Such an arrival, with comparable amplitudes in both transverse and vertical components, absent in the synthetics, apparently cannot be explained without recourse to effects of lateral heterogeneities in earth structure. Source complexity, within the prescribed fault plane, is an inadequate explanation, since, in a plane-layered structure, station 2 is nearly a node for vertical motion for both strike slip and dip slip.

In particular, because of the similarity of amplitude of the two components at station 2, it seems that no explanations can be made concerning the late-arriving phase as low group velocity surface waves generated by shallow slip on a distant segment of the fault. The long period of the phase also argues against shallow slip as the mechanism. Similar late-arriving phases, with about the same amplitude, occur at the other stations and are absent in the synthetics. The possible role of instrumental or processing error in explaining these late-time waveforms were not investigated.

In general, the synthetics seem to have a slightly higher frequency content than the data. A slower rupture velocity or slower surface layers might improve the agreement somewhat.

SUMMARY

A procedure for synthesizing earthquake ground motion was described incorporating both a dynamic model of faulting and the effects of geological structure. The key to computational efficiency is the partitioning of the problem into a source calculation and a wave-propagation calculation. It is evident that even though computation of the source function requires a three-dimensional treatment, the propagation of waves with a reasonable frequency resolution is not only expensive in three dimensions but also unnecessary. By observing that the azimuthal component of the radiated field from a double-couple point source is known and is not coupled to the radial or vertical components, the wave propagation was reduced, i.e., the computation of the Green's function in our prescribed layered medium, to a two-dimensional problem.

As an application of this method, an attempt was made to synthesize the near-field displacement records of the 1966 Parkfield earthquake. Although the data was not reproduced in detail, synthetic records were produced that were in overall agreement with the data. On the basis of this agreement, estimates show that the 1966 Parkfield earthquake had an average slip of 43 cm with an effective stress of 25 bars. Assuming a shear modulus of 3.0×10^{11} dyne/cm², the seismic moment was approximated to be 2.3×10^{25} dyne-cm. This moment can be compared with the moment estimate of Tsai and Aki (1969) which ranged between 0.9 and 2.1×10^{25} dyne-cm. Source parameters determined by other researchers are compared in Table 2. Undoubtedly, earthquakes in general and the Parkfield event in particular, involve a much more complicated stress relaxation process than the simple one prescribed in this study. The calculation described here can be viewed as a starting point for more detailed models of faulting.

ACKNOWLEDGMENTS

We want to thank Gerald Frazier who wrote the original version of the finite element code (SWIS) used as the starting point for this work. We also want to thank Jim Brune for his counsel and the Institute of Geophysics and Planetary Physics, UCSD, LaJolla, California, where much of this work was completed

under National Science Foundation Contract ENV 7502939. We thank Drs. Al Lindh and Sam Harding, and especially Dr. Bill Bakun, for their suggested improvements in the text.

APPENDIX

A difficulty arises in the three-dimensional numerical scheme for treating frictional sliding when the instantaneous sliding direction is not restrained *a priori*. Physically, the frictional traction at a point on a slip surface should be required to contribute an acceleration in the direction opposed to the instantaneous slip velocity. However, application of this criterion in numerical time-stepping schemes is not straightforward because the particle velocity and acceleration are centered at different distinct times. This discrepancy is not trivial for it leads to unstable behavior if not remedied. Our solution to this problem, taken from Day (1977), leads directly to a numerical criterion for arresting slip at a node. The resulting stopping criterion is equivalent to the physical requirement that slip ceases at a node whenever the magnitude of the frictional force vector on the node exceeds the combined inertial and restoring force vector.

We assume that a fault surface $\Sigma(t)$ with unit normal $\hat{n}(\xi, t)$ is specified as a function of time. To simplify the subsequent discussion, we restrict Σ to lie in the plane $x_3 = 0$, thus $\hat{n}(\xi, t) = \hat{x}_3$. A tangential discontinuity in slip $s(\xi, t)$ with ξ on Σ is permitted across Σ . Continuity of the normal displacement and continuity of the traction across Σ are required. We also assume that the fault slip is asymmetric and equal twice the displacement, $s(\xi, t) = 2 u(\xi, t)$. Σ is assigned a tangential traction τ due to sliding friction.

$$\tau_f(\xi, t) = -S_F \hat{s}(\xi, t) \quad (\text{A1})$$

where \hat{s} is the unit vector of the slip velocity and S_F is the product of a sliding friction coefficient (assumed constant and the normal component of traction). We constrain S_F to be positive. Thus equation (A1) incorporates the physical motion that friction always opposes the slip velocity.

Let \dot{U}_i represent the nodal velocity component in the \hat{x}_i direction at a particular grid point on Σ . In the following, let t equal to $m\Delta t$ where Δt is the numerical time step and m is an integer. Abbreviate $\dot{U}\left(t + \frac{\Delta t}{2}\right)$ and $\dot{U}\left(t - \frac{\Delta t}{2}\right)$ by $\dot{U}(+)$ and $\dot{U}(-)$, respectively. Our explicit time stepping scheme leads to the following expression for the tangential components at $t + \frac{\Delta t}{2}$;

$$\dot{U}_i(+) = \dot{U}_i(-) - \Delta t M^{-1}[R_i(t) - Q_i(t) - T_i^f(t)] \quad (\text{A2})$$

for $i = 1, 2$. $R_i(t)$, $Q_i(t)$, and M are derived from the finite element quadrature (Frazier and Petersen, 1974). R_i represents the i th component of the nodal restoring force resulting from stresses within the medium; Q_i represents the i th component of the nodal damping force resulting from artificial viscosity; M is the mass associated with the node by virtue of diagonalization of the mass matrix. T_i^f is the i th component of the nodal frictional force and is determined by use of equation (A1).

The difficulty in constructing $T_i^f(t)$ to represent (A1) correctly is that the frictional force at time t depends on the direction of slip velocity at time t . Unfortunately, the

time stepping scheme yields nodal velocities at times $t \pm n \frac{\Delta t}{2}$. Simply using the direction of the slip velocity at $t - \frac{\Delta t}{2}$ to determine T_i^f at time t leads to unstable behavior.

A successful solution for $T_i^f(t)$ is constructed by using the average value of the slip velocity direction cosines at $t - \frac{\Delta t}{2}$ and $t + \frac{\Delta t}{2}$,

$$T_i^f(t) = -\frac{1}{2} AS_F [\gamma_i(+) + \gamma_i(-)] \tag{A3}$$

$i = 1, 2$. $\gamma_i(+)$ and $\gamma_i(-)$ are the direction cosines of the slip velocity vector at $t + \frac{\Delta t}{2}$ and $t - \frac{\Delta t}{2}$, respectively, and A is a positive constant with units of length squared which arises from the finite element quadrature. Substituting (A3) into (A2) gives a pair of nonlinear, coupled equations for the unknown velocity components $\dot{U}_1(+)$ and $\dot{U}_2(+)$

$$\dot{U}_1(+) = C_1 - B \frac{\dot{U}_1(+)}{[\dot{U}_1^2(+) + \dot{U}_2^2(+)]^{1/2}} \tag{A4}$$

$$\dot{U}_2(+) = C_2 - B \frac{\dot{U}_2(+)}{[\dot{U}_1^2(+) + \dot{U}_2^2(+)]^{1/2}} \tag{A5}$$

where we have grouped all quantities that are known at times t and $t - \frac{\Delta t}{2}$ into constants C_1 , C_2 , and B given by

$$C_1 = \dot{U}_1(-) - \Delta t M^{-1} [R_1(t) - Q_1(t) + \frac{1}{2} AS_F \gamma_1(-)] \tag{A6}$$

$$C_2 = \dot{U}_2(-) - \Delta t M^{-1} [R_2(t) - Q_2(t) + \frac{1}{2} AS_F \gamma_2(-)] \tag{A7}$$

$$B = \frac{1}{2} \Delta t M^{-1} AS_F. \tag{A8}$$

The system is solved by making the substitution $\dot{U}_1(+) = r \cos \Theta$ and $\dot{U}_2(+) = r \sin \Theta$ which produces

$$\dot{U}_1(+) = C_1 - B \operatorname{sgn} [\dot{U}_1(+)] / (1 + C_2^2 / C_1^2)^{1/2} \tag{A9}$$

$$\dot{U}_2(+) = C_2 - B \operatorname{sgn} [\dot{U}_2(+)] / (1 + C_1^2 / C_2^2)^{1/2} \tag{A10}$$

where $\operatorname{sgn} [x]$ is $+1$ for $x > 0$ and -1 for $x < 0$. Equations (A8) and (A9) provide a stable numerical scheme for updating the nodal velocities on the slip surface.

Since B is necessarily positive, there exists a condition on the constants B , C_1 , and C_2 such that a solution exists to the systems (A7) and (A8). The condition for the solution to exist is that

$$(C_1^2 + C_2^2)^{1/2} > B. \tag{A11}$$

This condition insures a consistency in sign between the left-hand side of (A9) and (A10) and the sgn function on the right-hand side. The condition (A11) allows the

slip velocity $\dot{U}_i(+)$ to exist, hence the converse

$$(C_1^2 + C_2^2)^{1/2} < B \quad (\text{A12})$$

becomes the stopping criterion. If (A12) holds, a nonzero slip velocity is inadmissible as a solution to (A9) and (A10). Multiplying (A12) by $M/\Delta t$ and noting the definitions (A6), (A7), and (A8), we arrive at the physical interpretation: sliding ceases at a node when the magnitude of the frictional force would otherwise exceed the combined inertial and restoring forces.

REFERENCES

- Aki, K. (1968). Seismic displacements near a fault, *J. Geophys. Res.* **73**, 5339–5376.
- Aki, K. (1969). Seismic coda of local earthquakes, *J. Geophys. Res.* **74**, 615–631.
- Allen, C. R. and S. W. Smith (1966). Pre-earthquake and post-earthquake surficial displacements, *Bull. Seism. Soc. Am.* **56**, 966–967.
- Anderson, J. (1974). A dislocation model for the Parkfield earthquake, *Bull. Seism. Soc. Am.* **64**, 671–686.
- Archuleta, R. J. (1976). Experimental and numerical three-dimensional simulations of strike-slip earthquakes, *Ph.D. Dissertation*, University of California, San Diego.
- Archuleta, R. J. and G. A. Frazier (1978). Three-dimensional numerical simulations and dynamic faulting in a half-space, *Bull. Seism. Soc. Am.* **68**, 573–598.
- Ben-Menahem, A. (1961). Radiation of seismic surface-waves from finite sources, *Bull. Seism. Soc. Am.* **51**, 401–435.
- Boore, D. M., K. Aki, and T. Todd (1971). A two-dimensional moving dislocation model for a strike-slip fault, *Bull. Seism. Soc. Am.* **61**, 177–194.
- Burridge, R. and L. Knopoff (1964). Body force equivalents for seismic dislocations, *Bull. Seism. Soc. Am.* **54**, 1901–1914.
- Cloud, W. K. and V. Perez (1967). Accelerograms—Parkfield earthquake, *Bull. Seism. Soc. Am.* **57**, 1179–1192.
- Day, S. M. (1977). Finite element analysis of seismic scattering problems, *Ph.D. Dissertation*, University of California, San Diego.
- Eaton, J. P., A. E. O'Neil, and J. N. Murdock (1970). Aftershocks of the 1966 Parkfield-Cholame, California earthquake: a detailed study, *Bull. Seism. Soc. Am.* **60**, 1151–1197.
- Frazier, G. A. and C. M. Petersen (1974). 3-D stress wave code for the ILLIAC IV, Systems, Science, and Software Report SSS-R-74-2103.
- Haskell, N. A. (1969). Elastic displacements in the near-field of a propagating fault, *Bull. Seism. Soc. Am.* **59**, 865–908.
- Housner, G. W. and M. D. Trifunac (1967). Analysis of accelerograms—Parkfield earthquake, *Bull. Seism. Soc. Am.* **57**, 1193–1220.
- Levy, N. A. and A. K. Mal (1976). Calculation of general motion in a three-dimensional model of the 1966 Parkfield earthquake, *Bull. Seism. Soc. Am.* **66**, 405–423.
- Maryuama, T. (1963). On the force equivalents of dynamical elastic dislocations with reference to the earthquake mechanism, *Bull. Earthquake Res. Inst., Tokyo Univ.* **41**, 467–486.
- Mansinha, L. (1964). The velocity of shear fracture, *Bull. Seism. Soc. Am.* **54**, 369–376.
- McEvelly, T. V. (1966). Preliminary seismic data, June–July 1966 in Parkfield earthquakes of June 27–29, 1966, Monterey and San Luis Obispo Counties, California—Preliminary report, *Bull. Seism. Soc. Am.* **56**, 967–971.
- McEvelly, T. V., W. H. Bakun, and K. B. Casaday (1967). The Parkfield California earthquake of 1966, *Bull. Seism. Soc. Am.* **57**, 1221–1244.
- McNally, K. and T. V. McEvelly (1977). Velocity contrast across the San Andreas fault in central California: Small-scale variations from *P*-wave nodal plane distortion, *Bull. Seism. Soc. Am.* **67**, 1565–1576.
- Smith, S. W. and M. Wyss (1968). Displacement on the San Andreas fault subsequent to the 1966 Parkfield earthquake, *Bull. Seism. Soc. Am.* **58**, 1955–1973.
- Trifunac, M. D. (1971). Zero baseline correction of strong-motion accelerograms, *Bull. Seism. Soc. Am.* **61**, 1201–1211.
- Trifunac, M. D. and D. E. Hudson (1970). Analysis of the station no. 2 seismoscope record—1966, Parkfield, California earthquake, *Bull. Seism. Soc. Am.* **60**, 785–794.

- Tsai, Y. and K. Aki (1969). Simultaneous determination of the seismic moment and attenuation of seismic surface waves, *Bull. Seism. Soc. Am.* **59**, 275-287.
- Wu, F. T. (1968). Parkfield earthquake of June 28, 1966: magnitude and source mechanism, *Bull. Seism. Soc. Am.* **58**, 689-709.

U.S. GEOLOGICAL SURVEY
345 MIDDLEFIELD ROAD
MENLO PARK, CALIFORNIA 94025
(R.J.A.)

SYSTEMS, SCIENCE AND SOFTWARE
POST OFFICE BOX 1620
LA JOLLA, CALIFORNIA 92038
(S.M.D.)

Manuscript received October 26, 1979